Improved Nonaqueous Synthesis of TiO_2 for Dye-Sensitized Solar Cells

Morgan Stefik,[†,*] Florian J. Heiligtag,[§] Markus Niederberger,[§] and Michael Grätzel[‡]

[†]Department of Chemistry and Biochemistry, University of South Carolina, Columbia, South Carolina 29208, United States, [‡]Institute of Chemical Sciences and Engineering, École Polytechnique Fédérale de Lausanne, Laboratory of Photonics and Interfaces, Station 6, CH-1015 Lausanne, Switzerland, and [§]Laboratory for Multifunctional Materials, Department of Materials, ETH Zürich, Wolfgang-Pauli-Strasse 10, 8093 Zürich, Switzerland

ABSTRACT Nonaqueous synthesis routes have emerged as a powerful platform for directly obtaining diverse metal oxide nanoparticles with high crystallinity and tunable compositions. The benzyl alcohol (BA) route, for example, has been applied toward dozens of oxides including binary, ternary, and even more complex multimetal systems. Here we compare anatase nanoparticles made from the BA route with the traditional hydrothermal route. XPS measurements indicated that the BA route resulted in more reduced Ti states, corresponding to additional oxygen vacancies. These defects resulted in additional trap states, slower recombination, and slower charge transport. The performance of BA anatase was improved by incorporating niobium intended to suppress oxygen vacancies. The higher performance Nb-containing films were post-treated to yield a 7.96% power conversion efficiency (AM 1.5), similar to the state-of-the-art hydrolytic TiO_2 in the same configuration.

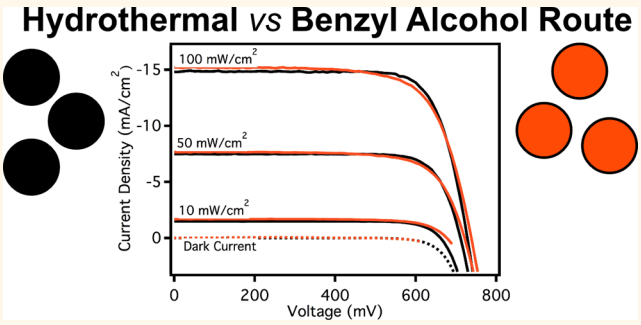

KEYWORDS: anatase nanoparticle · dye-sensitized solar cell · benzyl alcohol · nonhydrolytic

The rise of nanomaterials has led to significant advances in a broad range of (photo)electrochemical and (photo)catalytic applications where high interfacial surface areas are crucial for high reaction rates.[1−3] In the past decades, numerous synthesis routes have emerged for the controlled synthesis of diverse nanoparticles with control over the nominal size, crystallinity, faceting, and surface functionality.[4] Much focus has been turned toward transition metal oxide nanoparticles with a wide range of applications including batteries, fuel cells, supercapacitors, and photovoltaics. Access to crystalline transition metal oxide nanoparticles is often crucial to realize efficient devices with suitable carrier transport or photocatalytic activity, for example.[5,6] Water-based nanoparticle synthesis procedures, based on hydrolysis and condensation reactions, are quite popular due to the ease and low-cost for numerous oxide systems.[7] The products are oftentimes amorphous and much work has been devoted to subsequent crystallization with high-pressure or high-temperature treatments to obtain crystalline nanoparticles.[8,9] Nonaqueous, or nonhydrolytic, methods have more recently emerged as an alternative approach for synthesizing transition metal oxide nanoparticles that can enable crystalline products directly, often with lower temperatures and easier incorporation of multiple components.[10,11] The benzyl alcohol (BA) route has emerged as a unique and robust nonhydrolytic synthesis platform for a diverse range of single- and multimetal oxide nanoparticles,[12] and can notably lead to the synthesis of anatase TiO_2 close to room temperature.[13] The BA route includes numerous different reaction pathways that make it compatible with a wide gamut of metal precursor chemistries including chlorides, alkoxides, acetates, and acetylacetonates.[14]

Dye-sensitized solar cells (DSC) are low-cost photovoltaic devices based upon a sensitizing dye monolayer adsorbed on a high-surface area film of oxide nanoparticles.[1,15] Since the inception of the DSC in the early 1990s, anatase titania nanoparticles have remained the highest performance anode material. Here, a hydrolytic synthesis followed by a hydrothermal (HT)

* Address correspondence to morgan@stefikgroup.com.

Received for review July 9, 2013 and accepted September 9, 2013.

Published online September 09, 2013
10.1021/nn403500g

crystallization of anatase nanoparticles is the most popular and has led to the highest efficiency devices to date.[16] The optimized nanoparticle synthesis for DSCs involves a time-consuming set of 7 steps to obtain purified, crystalline anatase particles.[17] In contrast, the benzyl alcohol route significantly reduces the steps to just reagent mixing, heating, and centrifugation. Although there are a few reports of DSCs made from benzyl alcohol derived anatase, the influence of this unique synthesis route on the electronic properties of the particles has yet to be elucidated.[18−21] BA is known to be slightly reducing, sometimes even leading to the formation of suboxide nanoparticles,[22−24] metallic nanoparticles,[25] or bulk metals.[26] The reducing tendency of BA may in some cases favor the formation of reduced point defects such as oxygen vacancies. Such defects significantly alter the optoelectronic properties and strongly influence the performance of DSCs by modifying the charge injection, charge collection efficiency, and charge recombination rate.[27,28]

Here we examine the optoelectronic characteristics of BA derived anatase in comparison to the standard hydrothermal anatase that has been optimized for more than 20 years. We find significant differences in the trap state distributions, recombination rates, and charge transport rates that should be considered when designing new DSC photoanodes. The performance of BA anatase in DSCs was significantly improved by incorporating niobium intended to suppress the trap states. We show that a further postsynthesis treatment of Nb doped BA anatase leads an 11 μm thick transparent photoanode to have 7.96% power conversion efficiency that is similar to the state-of-the-art hydrolytic TiO_2, in the same configuration. These new relationships of synthesis parameters to optoelectronic properties and DSC performance give additional pathways forward for improved synthesis of DSC photoanodes.

RESULTS AND DISCUSSION

Anatase nanoparticles were prepared from benzyl alcohol for comparison with the standard hydrothermal route. Two types of nanoparticles were prepared from the BA route, including one pure sample ("BA TiO_2") and another containing Nb^{5+} ("BA Nb:TiO_2"), motivated *vida infra*. The synthesis parameters were systematically varied to yield similar particle sizes to the standard ∼20 nm nanoparticles used for DSCs. The nominal as-made particle size was determined with Scherrer analysis[29] to be 16.0 and 17.8 nm for the BA TiO_2 and BA Nb:TiO_2, respectively (Table 1, Figure S1). The BA Nb:TiO_2 particles were a deep blue color as-made, indicative of active donor levels below the conduction band (Figure 2d).[27,30] The blue color of as-made Nb:TiO_2 was found to be unstable and disappeared upon long-term particle storage or high temperature heat treatment in air, consistent with the findings of others where heat treatments in vacuum were needed to preserve the electrical conductivity from Nb doping of TiO_2,[31,32] whereas heat treatments in air deactivated the dopant and led to nonconductive films.[27] These findings highlight the often critical role of atmospheric oxygen in oxide defect chemistry.[33]

The nanoparticles were prepared into viscous pastes for the fabrication of mesoporous films. The porosity and average crystal size were characterized by nitrogen physisorption, XRD, and SEM. BET analysis of the physisorption data indicated that the films all had similar high surface areas of 60−84 m^2/g, corresponding to calculated average particle sizes of 18.4, 19.8, and 25.5 nm for the HT TiO_2, BA TiO_2, and BA Nb:TiO_2 (Table 1). The film porosities were also comparable with 59.5−64.9 vol % porosity. BJH analysis of the physisorption data indicated similar pore size distributions covering from ∼20−40 nm for the three films, with slightly larger pores for the BA Nb:TiO_2, corresponding to its larger particle size (Figure 1d). The XRD patterns after calcination were consistent with pure anatase phase for all the BA samples and only a slight trace of rutile was detected in HT TiO_2. Scherrer analysis was consistent with moderate grain growth, with average grain sizes of 16.4, 19.4, and 23.1 nm, respectively, for the three samples (Figure 1c, Table 1). The average domain size increased by 19% for BA TiO_2, whereas BA Nb:TiO_2 increased by 30%. This observation is counter to previous reports showing that Nb stabilizes anatase and retards grain growth.[34,35] The SEM micrographs showed a homogeneously random pore network and were consistent with the other particle dimensions, measuring 18.9 ± 4.3 and 24.0 ± 6.2 nm for BA TiO_2 and BA Nb:TiO_2, respectively (Figure 1a,b).

Further insights into the synthesis-property relationships were determined by measuring the surface binding energy distributions with X-ray photoelectron spectroscopy (XPS). The titanium $2p_{1/2}$ and $2p_{3/2}$ spectra are shown in Figure 2a. For all samples, the predominant peaks correspond to the Ti^{4+} oxidation state of TiO_2 with peaks near 459.0 and 464.8 eV of binding energy. Suboxides with reduced titanium oxidation states were apparent in several of the spectra, particularly near 454.6 and 462.7 eV so the spectra were deconvoluted to quantify the Ti_2O_3 (457.3 and 462.7 eV) and TiO (454.6 and 460.2 eV) observed at lower binding energies.[36] Although the observed peak near 454.6 eV was intermediate between reported binding energies of TiO (455.0 eV) and Ti metal (454.1 eV),[37] this peak was attributed to TiO after considering the high temperature calcinations in air. The Ti oxidation state distribution was calculated for each sample and is shown in Table 2 and Figures S2−S6. The HT synthesis route resulted in the most Ti^{4+} rich film, having 95.28

TABLE 1. Characteristics of Nanoparticles and Resulting Films

sample	BET surface area (m^2/g)	porosity volume (%)	BET particle size (nm)	XRD domain size[a] (nm)	XRD domain size[b] (nm)	dye-loading (#/nm^2)
HT TiO_2	83.8	68.0	18.4		16.4	0.47
BA TiO_2	78.1	59.5	19.8	16.0	19.4	0.41
BA Nb:TiO_2	60.3	64.9	25.5	17.8	23.1	0.37

[a] Average domain size for as-synthesized nanoparticles was determined by Scherrer analysis of the (101) and (200) peaks. [b] Average domain size for calcined nanoparticle films were calculated by the same method as 1.

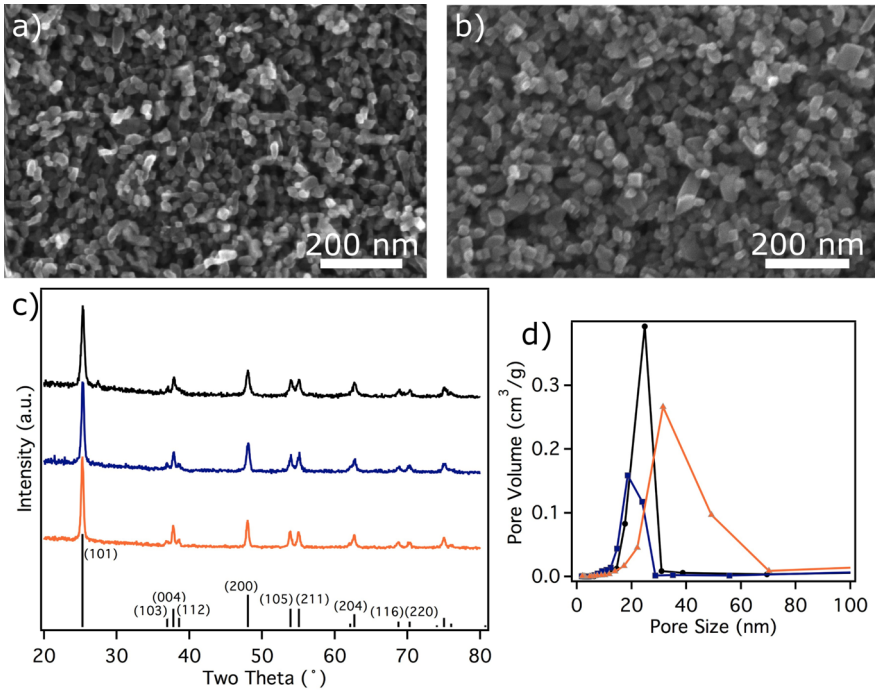

Figure 1. SEM micrographs of BA TiO_2 (a) and BA Nb:TiO_2 (b). XRD patterns for all calcined films (c) were shifted vertically for clarity and compared to anatase titania (PDF #21-1272). BJH pore volume distributions as a function of pore size (d). Plotted data correspond to HT TiO_2 (black), BA TiO_2 (blue), and BA Nb:TiO_2 (orange).

atom %. The as-made particles from the BA route were the most reduced, having 93.88 and 92.33 atom % Ti^{4+} for the pure and Nb-containing samples, respectively, consistent with a slightly reducing effect from the benzyl alcohol. In both cases, the subsequent calcination of BA derived particles in air increased the amount of Ti^{4+} to 94.56 and 94.76 atom %, respectively. We previously observed the deactivation of active Nb donor sites upon calcination in air and attributed this effect to the formation of Ti vacancies (eq 1).[27] Ti vacancies could form Schottky pairs with O vacancies and annihilate each other (eq 2). This is analogous to the excess oxygen associated with the Nb^{5+} filling oxygen vacancies.[38]

$$\frac{1}{2}Nb_2O_5 \xrightarrow{TiO_2} Nb_{Ti}^{\bullet} + \frac{1}{4}V_{Ti}^{''''} + \frac{5}{2}O_O^X \quad (1)$$

$$V_O^{\bullet\bullet} + \frac{1}{2}V_{Ti}^{''''} \leftrightarrow 0 \quad (2)$$

Such a mechanism could explain the slightly less reduced character of the Ti in BA Nb:TiO_2 compared to BA TiO_2 after calcination. Although all crystalline lattices have some intrinsic thermal disorder with a specific equilibrium vacancy concentration,[33,39] the specific preparatory conditions can have lasting effects[36,38,40,41] when there are slow kinetics for vacancy formation/elimination. The oxygen 1s spectra showed no significant differences between the samples except for the shoulder near 532−533 eV corresponding to hydroxyl groups, chemisorbed oxygen or adsorbed water[42] (Figure 2b). The O 1s spectra was not used to quantify the average Ti oxidation state due to this presence of diverse oxygen containing surface species in the signal. XPS was however used to confirm the 0.63 atom % Nb content of sample BA Nb:TiO_2, similar to the 0.5 atom % Nb used in the synthesis (Figure 2c). The electronic defect states resulting from each nanoparticle preparation method were distinct and should be anticipated to effect DSC performance.

Dye-sensitized solar cells were prepared to compare the optoelectronic characteristics of the different nanoparticle synthesis routes. No performance enhancing scattering layers or antireflection coatings were used

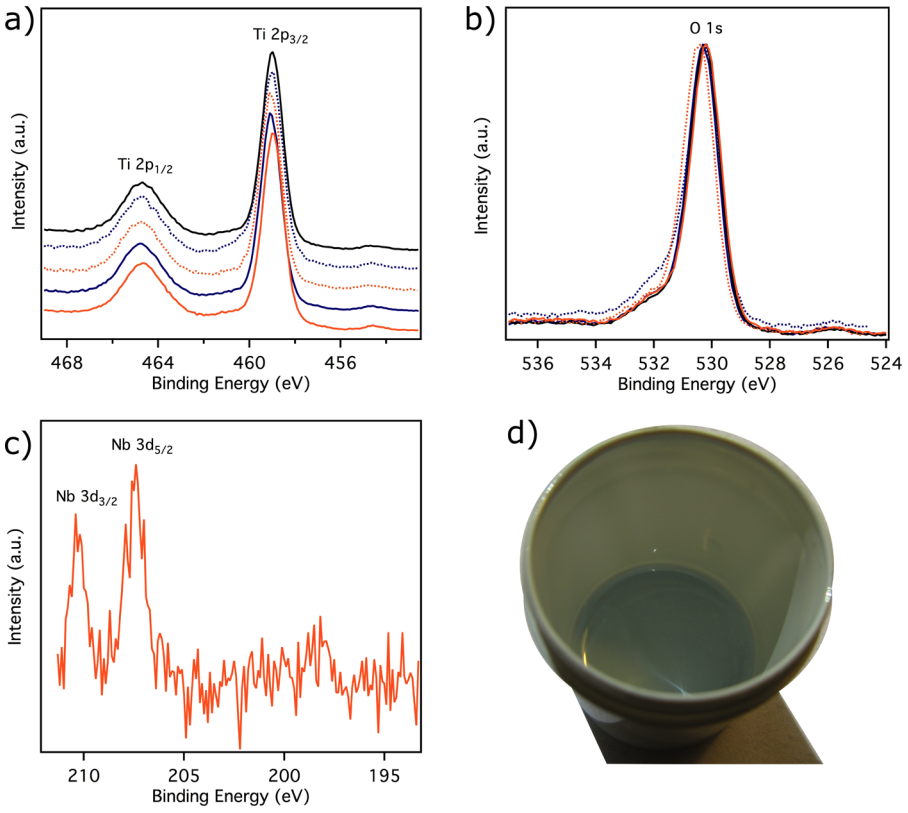

Figure 2. XPS binding energy distributions for Ti (a), O (b), and Nb (c) from samples HT TiO_2 (black), BA TiO_2 (blue), and BA Nb:TiO_2 (orange) along with the as-made nanoparticles (dashed lines). Spectra in (a) were shifted vertically for clarity. Photograph of freshly prepared BA Nb:TiO_2 paste with a blue color (d).

TABLE 2. Distribution of Ti Oxidation States in Calcined Films and As-Made Nanoparticles, Shown in Atomic Percentage

sample	TiO_2	Ti_2O_3	TiO
HT TiO_2	95.28	2.69	2.03
BA TiO_2 as-made	93.88	3.52	2.60
BA Nb: TiO_2 as-made	92.33	4.28	3.39
BA TiO_2	94.56	3.12	2.31
BA Nb:TiO_2	94.76	2.54	2.70

since the objective was to compare electronic properties. The DSCs made with the optimized hydrothermal route gave high power conversion efficiencies of 8.29% under 1 sun of illumination, with a short-circuit photocurrent of 14.7 mA/cm^2 and an open-circuit voltage of 728 mV (Figure 3, Table 3). The DSCs from BA TiO_2 yielded a modest power conversion efficiency of 5.42%, lower than that of the HT TiO_2 principally due to the reduced photocurrent of 10.1 mA/cm^2. The dye-desorption measurements indicated a similar content of C101 dye 0.47 *vs* 0.41 #/nm^2 for HT TiO_2 and BA TiO_2 (Table 1), respectively, indicating that the lowered photocurrent is due to either lowered electron injection from the excited dye state or a lowered electron collection efficiency. Niobium modification of anatase DSC photoanodes[38,43] was previously shown to enhance the charge collection efficiency with as little as

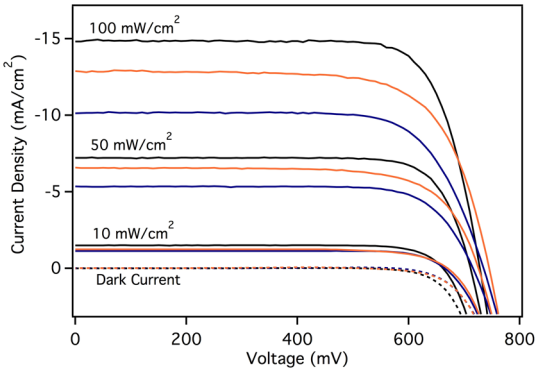

Figure 3. DSC JV curves for HT TiO_2 (black), BA TiO_2 (blue) and BA Nb:TiO_2 (orange) at 100, 50, 10, and 0% intensity of simulated AM 1.5 sunlight.

0.5 atom % Nb[27] so we investigated whether a similar approach could enhance BA derived TiO_2. The DSCs prepared from BA Nb:TiO_2 clearly showed a much improved efficiency of 6.78% under 1 sun of illumination, largely due to the increased short-circuit current of 12.8 mA/cm^2. The trends in performance were similar at reduced illumination intensities with power conversion efficiencies of 7.93, 6.08, and 6.54% for HT TiO_2, BA TiO_2, and BA Nb:TiO_2, respectively, under 10% simulated sunlight intensity. Both of the BA derived films exhibited smaller slopes for the photocurrent near V_{oc}, indicative of a higher series resistance

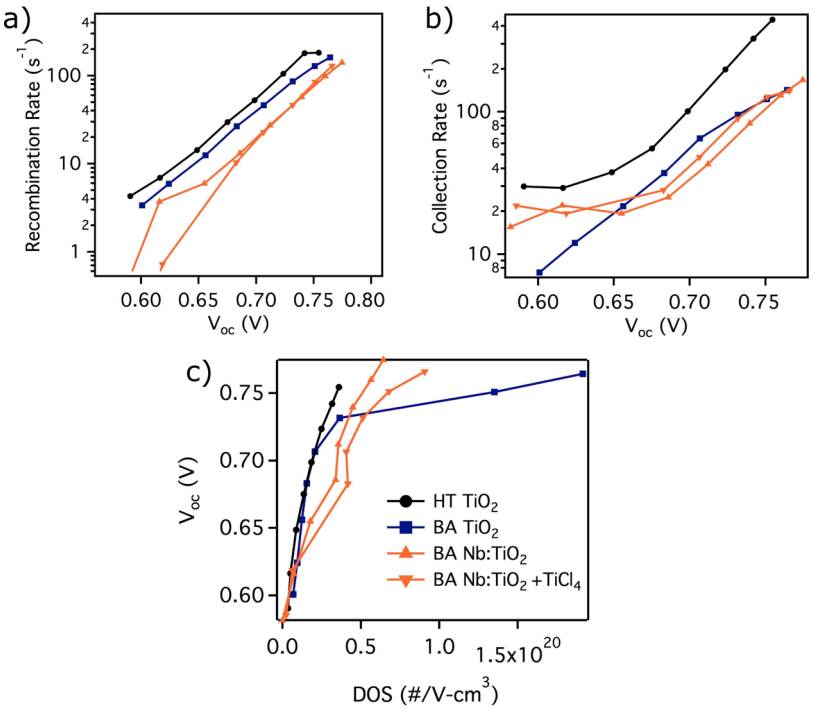

Figure 4. Transient photovoltage (a) and photocurrent (b) measurements were used to calculate the voltage dependent density of states (c) for samples HT TiO_2 (black circle), BA TiO_2 (blue square), BA Nb:TiO_2 (orange up-triangle), and BA Nb:TiO_2 + $TiCl_4$ (orange down-triangle).

compared to HT TiO_2. Further measurements were performed to investigate the sources of synthesis dependent DSC performance.

Transient photovoltage/current experiments enabled quantitative comparisons of the electron recombination and collection dynamics as a function of the anatase synthesis route. The transport of electrons in TiO_2 occurs *via* a trapping−detrapping mechanism from subbandgap states,[44] whereas recombination scales with the electron density and is sensitive to the trap state distribution.[45] Thus, overall device performance is strongly influenced by the specific TiO_2 trap state distribution. The fast relaxation of photovoltage transients indicated that the HT TiO_2 was the most active for recombination at a given V_{oc} (Figure 4a). The BA TiO_2 had a slightly reduced recombination rate and the BA Nb:TiO_2 had the slowest recombination rate, a factor of ∼2 less than HT TiO_2. These reduced recombination rates for the BA route were matched by similarly reduced electron transport rates, having a counter effect on the overall charge collection efficiency (Figure 4b). Oxygen vacancies are generally charge compensated by Ti^{3+} states in anatase that are known to form deep trap states ∼0.7−0.8 eV below the conduction band[46−49] and are anticipated to slow down electron transport. Thus, the slower electron transport in BA derived TiO_2 is consistent with the slightly reducing BA synthesis route. Further differences in the trap state distribution were evidenced by transient capacitance−voltage measurements, allowing for the calculation of the density of states (DOS) (Figure 4c). When the Nb-free samples are compared, it is clear that BA TiO_2 has significantly more trap states than HT TiO_2 at a given voltage, with more than 5 times at 0.75 V. Such changes in the DOS can be caused by either new states or a shift of the bands due to a surface dipole. This latter possibility was excluded by Mott−Schottky analysis of the Nb-free films showing similar flat band voltages (Figure S7). Beyond influencing transport and recombination, subbandgap states also can influence electron injection from the dye. Ideally the states are located at low enough energy levels to favor electron injection; however, this benefit must be matched accordingly to optimize the trade-off between enhanced photocurrent and reduced voltage.[50] Comparing the DSC performance data in Table 3, it is clear that the excess states in BA TiO_2 did not improve the photocurrent, but rather decreased the charge collection efficiency. As discussed, the addition of Nb can passivate oxygen vacancies and this effect was evidenced by the significantly narrowed DOS for BA Nb:TiO_2. In contrast to BA TiO_2, the Mott−Schottky analysis of BA Nb:TiO_2 showed a significant −45 mV shift in the flat band potential, similar to the −80 mV shift reported for $TiCl_4$ post treatments.[51,52] When correcting for this shift is done, the trap state distribution for BA Nb:TiO_2 is very similar to that of HT TiO_2 (Figure S8). The similar recombination and charge collection rates for the BA samples suggest that the addition of Nb coinciding with an increased photocurrent is due to enhanced electron injection from the dye, as supported by the

TABLE 3. Comparison of DSC Performance Metrics with Different Anatase Nanoparticles

	HT TiO_2	HT TiO_2	HT TiO_2	BA TiO_2	BA TiO_2	BA TiO_2	BA Nb: TiO_2	BA Nb: TiO_2	BA Nb: TiO_2
Intensity (% sun)	99.1	50.7	9.4	99.6	51.2	9.4	99.6	50.8	9.4
V_{oc} (mv)	728	711	661	735	716	664	745	725	669
J_{sc} (mA/cm^2)	14.7	7.6	1.4	10.1	5.5	1.1	12.8	6.7	1.3
Fill Factor (%)	76.8	78.5	79.8	72.8	75.7	81.5	70.7	71.9	73.0
Efficiency (%)	8.29	8.38	7.93	5.42	5.79	6.08	6.78	6.86	6.54

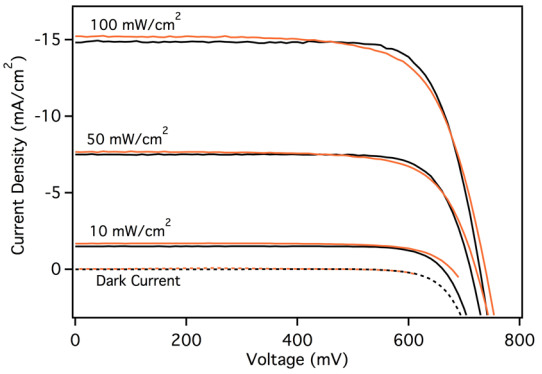

Figure 5. DSC JV curves of $TiCl_4$ treated Nb:TiO_2 (orange) compared to optimized HT TiO_2 (black) at 100, 50, 10, and 0% intensity of simulated AM 1.5 sunlight.

greater density of traps at low energy from 0.67 to 0.72 V. The explored synthetic routes for TiO_2 were found to have pronounced effects on the device performance and were correlated to different electron kinetics and trap state distributions.

The surface treatment of TiO_2 photoanodes is well-known to improve DSC performance. Chemical bath deposition of aqueous $TiCl_4$ is perhaps the most studied and operates by shifting the TiO_2 conduction band down 80 mV to improve charge injection from the dye while simultaneously reducing the recombination rate.[51,52] This highly optimized surface treatment was performed on our Nb:TiO_2 films to compare the performance of the two surfaces. Notably, the transient photovoltage measurements indicate no reduction in the recombination rates after $TiCl_4$ treatment of BA Nb:

TABLE 4. DSC Performance Metrics for BA Nb:TiO_2 after $TiCl_4$ Treatment

	BA Nb:TiO_2 + $TiCl_4$	BA Nb:TiO_2 + $TiCl_4$	BA Nb:TiO_2 + $TiCl_4$
Intensity (% sun)	99.6	52.7	12.2
V_{oc} (mv)	738	721	677
J_{sc} (mA/cm^2)	15.1	8.1	2.1
Fill Factor (%)	70.9	72.8	74.5
Efficiency (%)	7.96	8.0	8.4

TiO_2, indicating that the surface is already quite resistant to recombination (Figure 4a). Although the collection rate was unaffected, there was slight downward shift in the DOS (Figure 4b,c). These slight changes however, significantly improved the device performance to have 15.1 mA/cm^2 of short-circuit current and a power conversion efficiency of 7.96%, bringing the performance in line with the highly optimized HT TiO_2 (Figure 5, Table 4). These results are quite encouraging and show that alternative synthetic chemistries such as the benzyl alcohol route can lead to high performance devices. We anticipate that the limitless variations of related chemistries will lead to further DSC improvements.

CONCLUSION

We examined benzyl alcohol derived anatase nanoparticles in comparison with the optimized hydrothermal synthesis route. XPS measurements indicated that the BA synthesis route resulted in a greater quantity of reduced Ti oxidation states, corresponding to additional oxygen vacancies. This modified defect chemistry resulted in larger trap state distributions, slower recombination rates, and slower charge transport rates. The performance of BA derived anatase was significantly improved by incorporating niobium intended to suppress oxygen vacancies. These higher performance Nb-containing films were post-treated to yield a 7.96% power conversion efficiency (1 sun) that is similar to the state-of-the-art hydrolytic TiO_2 in the same configuration. The new relationships of synthesis parameters to electronic properties give additional pathways forward for the rational design of DSC photoanodes.

EXPERIMENTAL METHODS

Anatase Nanoparticle Synthesis. For undoped particles, 18.2 mmol (2.0 mL) of titanium tetrachloride (99.9%, Sigma-Aldrich) was added dropwise to 20 mL of benzyl alcohol (anhydrous, 99.8%, Sigma-Aldrich) and the mixture was reacted in an autoclave (Parr Acid Digestion Bombs, 45 mL) at 220 °C for 3 h. Without niobium, longer reaction times were found to result in the rutile polymorph. For doped particles, 4.55 mmol (0.5 mL) of titanium tetrachloride and 0.023 mmol (6.2 mg) of niobium pentachloride (99.95%, Alfa Aesar) were added to 20 mL of benzyl alcohol and the mixture was reacted in an autoclave at 220 °C for 48 h. As-made particles were purified by washing and centrifugation twice with chloroform and once with diethylether. Standard DSC anatase particles were prepared by a hydrolytic method as previously reported in detail.[17]

Paste Preparation. Viscous pastes were prepared from nanoparticle dispersions for screen printing as previously reported in detail.[17] In brief, nanoparticle dispersions in ethanol were combined with ethyl cellulose and terpineol. The mixture was agitated repeatedly with an ultrasonic horn and an Ultraturrax hand mixer before rotary evaporation to remove the ethanol. The resulting paste was heated to 75 °C for 1 h to remove trace ethanol and subjected to roll milling. Please note that it is crucial to use crystalline particles in paste preparation to avoid cracking and delamination during the calcination.

Material Characterization. Electron micrographs were acquired with a high-resolution scanning electron microscope (FEI XLF30

FEG and a Zeiss Merlin) with a through-the-lens detector for secondary electrons and 5 kV of accelerating voltage. Powder X-ray diffraction (XRD) patterns were acquired with a Bruker D8 Discover diffractometer, using monochromatic Cu Kα radiation (1.540598 Å) and a PANalytical X'Pert Pro diffractometer with Cu Kα radiation. The material binding energy distributions were probed using X-ray photoelectron spectroscopy (XPS) with an ESCA Kratos Axis Ultra, using the C peak at 285 eV to correct for sample charging. Additional Ti peaks were used for charging correction if the C peak was an asymmetric convolution. The XPS data were processed with CasaXPS 2.3.15 for deconvolution and integration of the overlapping peaks. Dye-uptake was measured by desorption in DMF containing tetrabutyl ammonium hydroxide and the resulting solution absorbance was measured by UV−visible spectrophotometry with a Hewlett-Packard 8452A diode array spectrophotometer. The surface area of the films were evaluated by the BET method using N_2 physisorption analysis at 77 K with a Micrometrics ASAP2000. Porosity distributions were calculated from the isotherms using the BJH method on the desorption branch to enhance sensitivity to necked pores. Prior to physisorption, the samples were degassed at 250 °C under vacuum for 4 h. Mott−Schottky type analysis was performed in pH 2 sulfuric acid after bubbling with dry nitrogen.[53] An Eco-Chimie Autolab PGSTAT 10 with an FRA module was used to record the impedance from −0.2 to 0.6 V *vs* Ag/AgCl at 1000 Hz. The recorded reactance was used to directly calculate the approximate capacitance as a function of voltage. The thicknesses of the screen-printed films were measured using a KLA Tencor alpha-step 500 surface profiler.

Device Fabrication. The NSG10 FTO photoanode glass was thoroughly cleaned and then treated twice with 40 mM $TiCl_4$ at 70 °C for 30 min. Anatase paste was applied to the glass by repeated screen printing to a nominal film thickness of 11 μm and calcined using a series of steps up to 500 °C.[17] Unless otherwise noted, the mesoporous photoanodes were as-made and not subjected to a subsequent surface treatment with $TiCl_4$. The photoanodes were sensitized in a heteroleptic ruthenium polypyridyl dye C101 complex[54] overnight at 4 °C as previously reported.[9] The dye solution contained 300 μM dye and 75 μM dineohexyl phosphinic acid (DINHOP) dissolved in equal volumes of acetonitrile and *tert*-butyl alcohol. The sensitized electrode was washed with acetonitrile and assembled. The counter electrode was prepared on TEC15 glass using an isopropyl alcohol solution of 5 mM H_2PtCl_6 and calcination to 410 °C for 15 min. The electrodes were thermally sealed together with a 25 μm thick Surlyn polymer seal. The electrolyte was injected through a hole in the counter electrode and was composed of 1 M DMII, 50 mM LiI, 30 mM I_2, 0.5 M *tert*-butyl pyridine, and 0.1 M GuNCS in a mixture of 85% acetonitrile and 15% valeronitrile. Further details on the reproducible assembly of high-efficiency DSCs were recently reported.[17]

Photovoltaic Characterization. A 450 W xenon lamp (Oriel) with an intensity of 100 mW/cm^2 was used to simulate AM 1.5 sunlight. The spectral output of the lamp was corrected with a Schott K113 Tempax sunlight filter (Präzisions Glas and Optik GmbH, Germany) to reduce the mismatch with the AM 1.5 spectrum to be less than 2%. Current−voltage characteristics were recorded with a digital source meter (Keithley model 2400). The photoactive area of 0.22 cm^2 was defined by a black metal mask to cut off stray light.[55] Plots of device IV characteristics were normalized to the intended illumination intensities and the non-normalized data are provided in tabular format. Multiple devices were measured for each condition, with the highest efficiency devices being reported. Please see Figure S9 for an indication of the typical statistical spread in performance metrics. Electron recombination and transport were measured by transient photovoltage and photocurrent decay measurements, respectively. The white light was generated by an array of LEDs, while a red LED light pulse was controlled by a solid-state switch. The transient measurements were recorded with a digital source meter (Keithly model 2602).

Conflict of Interest: The authors declare no competing financial interest.

Supporting Information Available: XRD of as-made particles, XPS deconvolutions, Mott−Schottky analysis, shifted DOS distributions, device statistics. This material is available free of charge *via* the Internet at http://pubs.acs.org.

Acknowledgment. The authors would like to thank Aravind Kumar Chandiran, Aswani Yella, and Hoi Nok Tsao for guidance with DSC fabrication and testing, Nicolas Xanthopoulos from the Centre Interdisciplinaire de Microscopie Electronique (CIME) at EPFL for XPS measurements and analysis, Pascal Comte for assistance with the paste preparation, S. M. Zakeeruddin for providing C101 dye and electrolyte solutions, and Thomas Moehl for discussions regarding impedance analysis. M.S. is grateful for financial support from the Swiss Commission for Technology and Innovation (CTI) (Award no. 13369.1 PFFLR-NM). M.G. acknowledges funding by the European Research Council (ERC) under the ERC-2009-AdG Grant no. 247404 MESO-LIGHT. F.J.H. and M.N. gratefully acknowledge financial support by ETH Zurich (ETH-07 09-2).

REFERENCES AND NOTES

1. O'Regan, B.; Grätzel, M. A Low-Cost, High-Efficiency Solar-Cell Based on Dye-Sensitized Colloidal TiO_2 Films. *Nature* **1991**, *353*, 737–740.
2. Zaluska, A.; Zaluski, L.; Strom-Olsen, J. O. Nanocrystalline Magnesium for Hydrogen Storage. *J. Alloys Compd.* **1999**, *288*, 217–225.
3. Arico, A. S.; Bruce, P.; Scrosati, B.; Tarascon, J. M.; Van Schalkwijk, W. Nanostructured Materials for Advanced Energy Conversion and Storage Devices. *Nat. Mater.* **2005**, *4*, 366–377.
4. Ozin, G. A.; Arsenault, A. C.; Royal Society of Chemistry. *Nanochemistry: A Chemistry Approach to Nanomaterials*; RSC Publishing: Cambridge, 2005; p 628.
5. Ohtani, B.; Ogawa, Y.; Nishimoto, S. Photocatalytic Activity of Amorphous-Anatase Mixture of Titanium(IV) Oxide Particles Suspended in Aqueous solutions. *J. Phys. Chem. B* **1997**, *101*, 3746–3752.
6. Guldin, S.; Huttner, S.; Tiwana, P.; Orilall, M. C.; Ulgut, B.; Stefik, M.; Docampo, P.; Kolle, M.; Divitini, G.; Ducati, C.; *et al.* Improved Conductivity in Dye-Sensitised Solar Cells through Block-Copolymer Confined TiO_2 Crystallisation. *Energy Environ. Sci.* **2011**, *4*, 225–233.
7. Brinker, C. J.; Scherer, G. W. *Sol-Gel Science: The Physics and Chemistry of Sol-Gel Processing*; Academic Press: Boston, MA, 1990; p 908.
8. Helgeson, H. C. Thermodynamics of Hydrothermal Systems at Elevated Temperatures and Pressures. *Am. J. Sci.* **1969**, *267*, 729.
9. Rajamathi, M.; Seshadri, R. Oxide and Chalcogenide Nanoparticles from Hydrothermal/Solvothermal Reactions. *Curr. Opin. Solid State Mater. Sci.* **2002**, *6*, 337–345.
10. Arnal, P.; Corriu, R. J. P.; Leclercq, D.; Mutin, P. H.; Vioux, A. A Solution Chemistry Study of Nonhydrolytic Sol-Gel Routes to Titania. *Chem. Mater.* **1997**, *9*, 694–698.
11. Vioux, A. Nonhydrolytic Sol-Gel Routes to Oxides. *Chem. Mater.* **1997**, *9*, 2292–2299.
12. Pinna, N.; Niederberger, M. Surfactant-Free Nonaqueous Synthesis of Metal Oxide Nanostructures. *Angew. Chem., Int. Ed.* **2008**, *47*, 5292–5304.
13. Niederberger, M.; Bartl, M. H.; Stucky, G. D. Benzyl Alcohol and Titanium Tetrachloride—A Versatile Reaction System for the Nonaqueous and Low-Temperature Preparation of Crystalline and Luminescent Titania Nanoparticles. *Chem. Mater.* **2002**, *14*, 4364–4370.
14. Niederberger, M.; Garnweitner, G. Organic Reaction Pathways in the Nonaqueous Synthesis of Metal Oxide Nanoparticles. *Chem.—Eur. J.* **2006**, *12*, 7282–7302.
15. Grätzel, M. Dye-Sensitized Solid-State Heterojunction Solar Cells. *MRS Bull.* **2005**, *30*, 23–27.
16. Yella, A.; Lee, H.-W.; Tsao, H. N.; Yi, C.; Chandiran, A. K.; Nazeeruddin, M. K.; Diau, E. W.-G.; Yeh, C.-Y.; Zakeeruddin, S. M.; Grätzel, M. Porphyrin-Sensitized Solar Cells with Cobalt (II/III)-Based Redox Electrolyte Exceed 12% Efficiency. *Science* **2011**, *334*, 629–634.

17. Ito, S.; Murakami, T. N.; Comte, P.; Liska, P.; Graetzel, C.; Nazeeruddin, M. K.; Grätzel, M. Fabrication of Thin Film Dye Sensitized Solar Cells with Solar to Electric Power Conversion Efficiency Over 10%. *Thin Solid Films* **2008**, *516*, 4613–4619.
18. Szeifert, J. M.; Fattakhova-Rohlfing, D.; Georgiadou, D.; Kalousek, V.; Rathousky, J.; Kuang, D.; Wenger, S.; Zakeeruddin, S. M.; Grätzel, M.; Bein, T. "Brick and Mortar" Strategy for the Formation of Highly Crystalline Mesoporous Titania Films from Nanocrystalline Building Blocks. *Chem. Mater.* **2009**, *21*, 1260–1265.
19. Melcarne, G.; De Marco, L.; Carlino, E.; Martina, F.; Manca, M.; Cingolani, R.; Gigli, G.; Ciccarella, G. Surfactant-Free Synthesis of Pure Anatase TiO_2 Nanorods Suitable for Dye-Sensitized Solar Cells. *J. Mater. Chem.* **2010**, *20*, 7248–7254.
20. De Marco, L.; Manca, M.; Giannuzzi, R.; Malara, F.; Melcarne, G.; Ciccarella, G.; Zama, I.; Cingolani, R.; Gigli, G. Novel Preparation Method of TiO_2-Nanorod-Based Photoelectrodes for Dye-Sensitized Solar Cells with Improved Light-Harvesting Efficiency. *J. Phys. Chem. C* **2010**, *114*, 4228–4236.
21. Szeifert, J. M.; Fattakhova-Rohlfing, D.; Rathousky, J.; Bein, T. Multilayered High Surface Area "Brick and Mortar" Mesoporous Titania Films as Efficient Anodes in Dye-Sensitized Solar Cells. *Chem. Mater.* **2012**, *24*, 659–663.
22. Pinna, N.; Grancharov, S.; Beato, P.; Bonville, P.; Antonietti, M.; Niederberger, M. Magnetite Nanocrystals: Nonaqueous Synthesis, Characterization, and Solubility. *Chem. Mater.* **2005**, *17*, 3044–3049.
23. Polleux, J.; Gurlo, A.; Barsan, N.; Weimar, U.; Antonietti, M.; Niederberger, M. Template-Free Synthesis and Assembly of Single-Crystalline Tungsten Oxide Nanowires and their Gas-Sensing Properties. *Angew. Chem., Int. Ed.* **2006**, *45*, 261–265.
24. Bilecka, I.; Djerdj, I.; Niederberger, M. One-Minute Synthesis of Crystalline Binary and Ternary Metal Oxide Nanoparticles. *Chem. Commun.* **2008**, 886–888.
25. Jia, F. L.; Zhang, L. Z.; Shang, X. Y.; Yang, Y. Non-Aqueous Sol−Gel Approach towards the Controllable Synthesis of Nickel Nanospheres, Nanowires, and Nanoflowers. *Adv. Mater.* **2008**, *20*, 1050–1054.
26. Kränzlin, N.; Ellenbroek, S.; Durán-Martín, D.; Niederberger, M. Liquid-Phase Deposition of Freestanding Copper Foils and Supported Copper Thin Films and Their Structuring into Conducting Line Patterns. *Angew. Chem., Int. Ed.* **2012**, *51*, 4743–4746.
27. Chandiran, A. K.; Sauvage, F.; Casas-Cabanas, M.; Comte, P.; Zakeeruddin, S. M.; Grätzel, M. Doping a TiO_2 Photoanode with Nb^{5+} to Enhance Transparency and Charge Collection Efficiency in Dye-Sensitized Solar Cells. *J. Phys. Chem. C* **2010**, *114*, 15849–15856.
28. Chandiran, A. K.; Sauvage, F.; Etgar, L.; Grätzel, M. Ga^{3+} and Y^{3+} Cationic Substitution in Mesoporous TiO_2 Photoanodes for Photovoltaic Applications. *J. Phys. Chem. C* **2011**, *115*, 9232–9240.
29. Scherrer, P. Bestimmung der Grösse und der Inneren Struktur von Kolloidteilchen mittels Röntgenstrahlen. *Nachr. Ges. Wiss. Goettingen, Math.−Phys. Kl.* **1918**, *2*, 98–100.
30. Kurita, D.; Ohta, S.; Sugiura, K.; Ohta, H.; Koumoto, K. Carrier Generation and Transport Properties of Heavily Nb-Doped Anatase TiO_2 Epitaxial Films at High Temperatures. *J. Appl. Phys.* **2006**, *100*, 1–3.
31. Hitosugi, T.; Yamada, N.; Nakao, S.; Hirose, Y.; Hasegawa, T. Properties of TiO_2-Based Transparent Conducting Oxides. *Phys. Status Solidi A* **2010**, *207*, 1529–1537.
32. Park, J.-H.; Kang, S. J.; Na, S.-I.; Lee, H. H.; Kim, S.-W.; Hosono, H.; Kim, H.-K. Indium-Free, Acid-Resistant Anatase Nb-Doped TiO_2 Electrodes Activated by Rapid-Thermal Annealing for Cost-Effective Organic Photovoltaics. *Sol. Energy Mater. Sol. Cells* **2011**, *95*, 2178–2185.
33. van de Krol, R.; Grätzel, M. *Photoelectrochemical Hydrogen Production*; Springer: New York, 2012; Vol. 102, p 321.
34. Arbiol, J.; Cerda, J.; Dezanneau, G.; Cirera, A.; Peiro, F.; Cornet, A.; Morante, J. R. Effects of Nb doping on the TiO_2 Anatase-to-Rutile Phase Transition. *J. Appl. Phys.* **2002**, *92*, 853–861.
35. Sotter, E.; Vilanova, X.; Llobet, E.; Stankova, M.; Correig, X. Niobium-Doped Titania Nanopowders for Gas Sensor Applications. *J. Optoelectron. Adv. Mater.* **2005**, *7*, 1395–1398.
36. Kim, S. R.; Parvez, M. K. Oxygen Ion-Beam Irradiation of TiO_2 Films Reduces Oxygen Vacancies and Improves Performance of Dye-Sensitized Solar Cells. *J. Mater. Res.* **2011**, *26*, 1012–1017.
37. Moulder, J. F.; Stickel, W. F.; Sobol, P. E.; Bomben, K. D. *Handbook of X-ray Photoelectron Spectroscopy*; Perkin-Elmer Corp: Norwalk, CT, 1992.
38. Nikolay, T.; Larina, L.; Shevaleevskiy, O.; Ahn, B. T. Electronic Structure Study of Lightly Nb-Doped TiO_2 Electrode for Dye-Sensitized Solar Cells. *Energy Environ. Sci.* **2011**, *4*, 1480–1486.
39. Callister, W. D. *Materials Science and Engineering: An Introduction*. 7th ed.; John Wiley & Sons: New York, 2007; p 721.
40. Etacheri, V.; Seery, M. K.; Hinder, S. J.; Pillai, S. C. Oxygen Rich Titania: A Dopant Free, High Temperature Stable, and Visible-Light Active Anatase Photocatalyst. *Adv. Funct. Mater.* **2011**, *21*, 3744–3752.
41. Tak Kim, J.; Ho Kim, S. Surface Modification of TiO_2 Electrode by Various Over-Layer Coatings and O_2 Plasma Treatment for Dye Sensitized Solar Cells. *Sol. Energy Mater. Sol. Cells* **2011**, *95*, 336–339.
42. Sanjines, R.; Tang, H.; Berger, H.; Gozzo, F.; Margaritondo, G.; Levy, F. Electronic-Structure of Anatase TiO_2 Oxide. *J. Appl. Phys.* **1994**, *75*, 2945–2951.
43. Lu, X. J.; Mou, X. L.; Wu, J. J.; Zhang, D. W.; Zhang, L. L.; Huang, F. Q.; Xu, F. F.; Huang, S. M. Improved-Performance Dye-Sensitized Solar Cells Using Nb-Doped TiO_2 Electrodes: Efficient Electron Injection and Transfer. *Adv. Funct. Mater.* **2010**, *20*, 509–515.
44. Nelson, J. Continuous-Time Random-Walk Model of Electron Transport in Nanocrystalline TiO_2 Electrodes. *Phys. Rev. B* **1999**, *59*, 15374–15380.
45. Nelson, J.; Haque, S. A.; Klug, D. R.; Durrant, J. R. Trap-Limited Recombination in Dye-Sensitized Nanocrystalline Metal Oxide Electrodes. *Phys. Rev. B* **2001**, *63*, 1–9.
46. Henrich, V. E.; Dresselhaus, G.; Zeiger, H. J. Observation of 2-Dimensional Phases Associated with Defect States on Surfaces of TiO_2. *Phys. Rev. Lett.* **1976**, *36*, 1335–1339.
47. Kim, W. T.; Kim, C. D.; Choi, Q. W. Sub-Band-Gap Photoresponse of TiO_2-X Thin-Film−Electrolyte Interface. *Phys. Rev. B* **1984**, *30*, 3625–3628.
48. Kumar, P. M.; Badrinarayanan, S.; Sastry, M. Nanocrystalline TiO_2 Studied by Optical, FTIR and X-ray Photoelectron Spectroscopy: Correlation to Presence of Surface States. *Thin Solid Films* **2000**, *358*, 122–130.
49. Morgan, B. J.; Watson, G. W. A DFT+U Description of Oxygen Vacancies at the TiO_2 Rutile (110) Surface. *Surf. Sci.* **2007**, *601*, 5034–5041.
50. Docampo, P.; Stefik, M.; Guldin, S.; Gunning, R.; Yufa, N. A.; Cai, N.; Wang, P.; Steiner, U.; Wiesner, U.; Snaith, H. J. Triblock-Terpolymer-Directed Self-Assembly of Mesoporous TiO_2: High-Performance Photoanodes for Solid-State Dye-Sensitized Solar Cells. *Adv. Energy Mater.* **2012**, *2*, 676–682.
51. Sommeling, P. M.; O'Regan, B. C.; Haswell, R. R.; Smit, H. J. P.; Bakker, N. J.; Smits, J. J. T.; Kroon, J. M.; van Roosmalen, J. A. M. Influence of a $TiCl_4$ Post-Treatment on Nanocrystalline TiO_2 Films in Dye-Sensitized Solar Cells. *J. Phys. Chem. B* **2006**, *110*, 19191–19197.
52. O'Regan, B. C.; Durrant, J. R.; Sommeling, P. M.; Bakker, N. J. Influence of the $TiCl_4$ Treatment on Nanocrystalline TiO_2 Films in Dye-Sensitized Solar Cells. 2. Charge Density, Band Edge Shifts, and Quantification of Recombination Losses at Short Circuit. *J. Phys. Chem. C* **2007**, *111*, 14001–14010.
53. Fabregat-Santiago, F.; Garcia-Belmonte, G.; Bisquert, J.; Bogdanoff, P.; Zaban, A. Mott-Schottky Analysis of Nanoporous Semiconductor Electrodes in Dielectric State

Deposited on SnO_2(F) Conducting Substrates. *J. Electrochem. Soc.* **2003**, *150*, E293–E298.
54. Gao, F.; Wang, Y.; Shi, D.; Zhang, J.; Wang, M.; Jing, X.; Humphry-Baker, R.; Wang, P.; Zakeeruddin, S. M.; Grätzel, M. Enhance the Optical Absorptivity of Nanocrystalline TiO_2 Film with High Molar Extinction Coefficient Ruthenium Sensitizers for High Performance Dye-Sensitized Solar Cells. *J. Am. Chem. Soc.* **2008**, *130*, 10720–10728.
55. Snaith, H. J. How Should You Measure Your Excitonic Solar Cells? *Energy Environ. Sci.* **2012**, *5*, 6513–6520.